Development and characterization of a ΔE-TOF detector prototype for the FOOT experiment

Matteo Morrocchi[a], Esther Ciarrocchi[b,a,*], Andrey Alexandrov[c], Behcet Alpat[d], Giovanni Ambrosi[d], Stefano Argirò[e,f], Raul Arteche Diaz[g,f], Nazar Bartosik[f], Giuseppe Battistoni[h], Nicola Belcari[b,a], Matteo Bertazzoni[b,1], Silvia Biondi[i,j], Graziano Bruni[i], Niccolò Camarlinghi[b,a], Pietro Carra[b,a], Piergiorgio Cerello[f], Alberto Clozza[k], Sofia Colombi[l,m], Giovanni De Lellis[c,n], Alberto Del Guerra[b,a], Micol De Simoni[o,p], Antonia Di Crescenzo[c,n], Marco Donetti[f,q], Yunsheng Dong[h,r], Marco Durante[l], Alessia Embriaco[h], Max Emde[s], Riccardo Faccini[o,p], Veronica Ferrero[e,f], Fernando Ferroni[p,o], Emanuele Fiandrini[d,t], Christian Finck[u], Elisa Fiorina[a,q], Marta Fischetti[v,p], Marco Francesconi[b,a], Matteo Franchini[i,j], Luca Galli[a], Marco Garbini[i,j,w], Valerio Gentile[x], Giuseppe Giraudo[f], Ronja Hetzel[s], Sebastian Hild[l], Maria Ionica[d], Keida Kanxheri[d,t], Aafke Christine Kraan[a], Valeria Lante[q], Adele Lauria[c,n], Chiara La Tessa[l,m], Ernesto Lopez Torres[g,f], Michela Marafini[w,p], Ilaria Mattei[h], Alberto Mengarelli[i], Riccardo Mirabelli[o,p,w], Maria Cristina Montesi[c,n], Maria Cristina Morone[y,z], Silvia Muraro[a], Livio Narici[y,z], Alessandra Pastore[aa], Nadia Pastrone[f], Vincenzo Patera[v,p,w], Francesco Pennazio[f], Pisana Placidi[d,ab], Marco Pullia[q], Luciano Ramello[f,ac], Riccardo Ridolfi[j], Valeria Rosso[b,a], Marta Rovituso[l], Claudio Sanelli[k], Alessio Sarti[v,k,w], Gabriella Sartorelli[i,j], Osamu Sato[ad], Simone Savazzi[q], Lorenzo Scavarda[e,f], Angelo Schiavi[v,p], Christoph Schuy[ae], Emanuele Scifoni[l], Adalberto Sciubba[v,p,w], Marco Selvi[i], Leonello Servoli[d], Gianluigi Silvestre[d,t], Mario Sitta[f,ac], Roberto Spighi[i], Eleuterio Spiriti[k], Giancarlo Sportelli[a,b], Achim Stahl[s], Sandro Tomassini[k], Francesco Tommasino[l,m], Giacomo Traini[o,p,w], Tioukov Valeri[c], Serena Marta Valle[r,h], Marie Vanstalle[u], Mauro Villa[i,j], Ulrich Weber[ae], Antonio Zoccoli[i,j], Maria Giuseppina Bisogni[b,a]

[a] *Istituto Nazionale di Fisica Nucleare (INFN), Section of Pisa, Pisa, Italy*
[b] *University of Pisa, Department of Physics, Pisa, Italy*
[c] *Istituto Nazionale di Fisica Nucleare (INFN), Section of Napoli, Napoli, Italy*
[d] *Istituto Nazionale di Fisica Nucleare (INFN), Section of Perugia, Perugia, Italy*
[e] *University of Torino, Department of Physics, Torino, Italy*
[f] *Istituto Nazionale di Fisica Nucleare (INFN), Section of Torino, Torino, Italy*
[g] *CEADEN, Havana, Cuba*
[h] *Istituto Nazionale di Fisica Nucleare (INFN), Section of Milano, Milano, Italy*
[i] *Istituto Nazionale di Fisica Nucleare (INFN), Section of Bologna, Bologna, Italy*
[j] *University of Bologna, Department of Physics and Astronomy, Bologna, Italy*
[k] *Istituto Nazionale di Fisica Nucleare (INFN), Laboratori Nazionali di Frascati, Frascati, Italy*
[l] *Trento Institute for Fundamental Physics and Applications, Istituto Nazionale di Fisica Nucleare (TIFPA-INFN), Trento, Italy*
[m] *University of Trento, Department of Physics, Trento, Italy*

[*] Corresponding author
[1] Currently employed at Derga Consulting Srl, Bolzano, Italy

[n] *University of Napoli, Department of Physics "E. Pancini", Napoli, Italy*
[o] *University of Roma La Sapienza, Department of Physics, Roma, Italy*
[p] *Istituto Nazionale di Fisica Nucleare (INFN), Section of Roma 1, Roma, Italy*
[q] *Centro Nazionale di Adroterapia Oncologica (CNAO), Pavia, Italy*
[r] *University of Milano, Department of Physics, Milano, Italy*
[s] *RWTH Aachen University, Physics Institute III B, Aachen, Germany*
[t] *University of Perugia, Department of Physics and Geology, Perugia, Italy*
[u] *Université de Strasbourg, CNRS, IPHC UMR 7871, F-67000 Strasbourg, France*
[v] *University of Roma La Sapienza, Department of Scienze di Base e Applicate per l'Ingegneria (SBAI), Roma, Italy*
[w] *Museo Storico della Fisica e Centro Studi e Ricerche Enrico Fermi, Roma, Italy*
[x] *Gran Sasso Science Institute, L'Aquila, Italy*
[y] *University of Roma Tor Vergata, Department of Physics, Roma, Italy*
[z] *Istituto Nazionale di Fisica Nucleare (INFN), Section of Roma 2, Roma, Italy*
[aa] *Istituto Nazionale di Fisica Nucleare (INFN), Section of Bari, Bari, Italy*
[ab] *University of Perugia, Department of Engineering, Perugia, Italy*
[ac] *University of Piemonte Orientale, Department of Science and Technological Innovation, Alessandria, Italy*
[ad] *Nagoya University, Department of Physics, Nagoya, Japan*
[ae] *Gesellschaft für Schwerionenforschung (GSI), Darmstadt, Germany*

Abstract

This paper describes the development and characterization of a ΔE-TOF detector composed of a plastic scintillator bar coupled at both ends to silicon photomultipliers. This detector is a prototype of a larger version which will be used in the FOOT (FragmentatiOn Of Target) experiment to identify the fragments produced by ion beams accelerated onto a hydrogen-enriched target. The final ΔE-TOF detector will be composed of two layers of plastic scintillator bars with orthogonal orientation and will measure, for each crossing fragment, the energy deposited in the plastic scintillator (ΔE), the time of flight (TOF), and the coordinates of the interaction position in the scintillator. To meet the FOOT experimental requirements, the detector should have energy resolution of a few percents and time resolution of 70 ps, and it should allow to discriminate multiple fragments belonging to the same event. To evaluate the achievable performances, the detector prototype was irradiated with protons of kinetic energy in the 70-230 MeV range and interacting at several positions along the bar. The measured energy resolution $\sigma_{\Delta E}/\Delta E$ was 6-14%, after subtracting the fluctuations of the deposited energy. A time resolution σ between 120 and 180 ps was obtained with respect to a trigger detector. A spatial resolution σ of 1.9 cm was obtained for protons interacting at the center of the bar.

Keywords: particle detectors, particle therapy, plastic scintillator, silicon photomultiplier

Introduction

Hadrontherapy is a form of external radiotherapy that uses beams of protons (protontherapy) or heavier particles (ion therapy, mainly ^{12}C) to treat tumors [1]. The typical energy range for therapeutic applications is 50-250 MeV for protons and 50-400 MeV/u for carbon ions. With respect to conventional radiotherapy with photons or electrons, the effectiveness of hadrontherapy is potentially improved by a better dose localization. However, nuclear interactions between the particle beams and the nuclei of the human body create ion fragmentation products [2, 3], ranging from protons to oxygen ions, with variable relative biological effectiveness (RBE) compared to conventional photon beams. A better understanding of the phenomena taking place during proton and hadrontherapy could improve the dose estimation in the treatment planning phase. In particular, target fragmentation in protontherapy causes the production of low energy, short-range fragments along the beam path in the patient [4] which could explain the difference between the measured proton RBE and its predicted value. Projectile fragmentation of carbon ions produces long-range forward-emitted secondary ions that release dose in the healthy tissue beyond the tumor target. Some experiments have recently been dedicated to studying projectile fragmentation for ^{12}C ions, such as the FIRST (Fragmentation of Ions Relevant for Space and Therapy) experiment [5]. However, only a few energies have been investigated [6, 7].

The FOOT (FragmentatiOn Of Target) experiment was recently proposed to study the fragmentation processes that occur in the human body during hadrontherapy [8, 9, 10]. In the target fragmentation induced by proton beams,

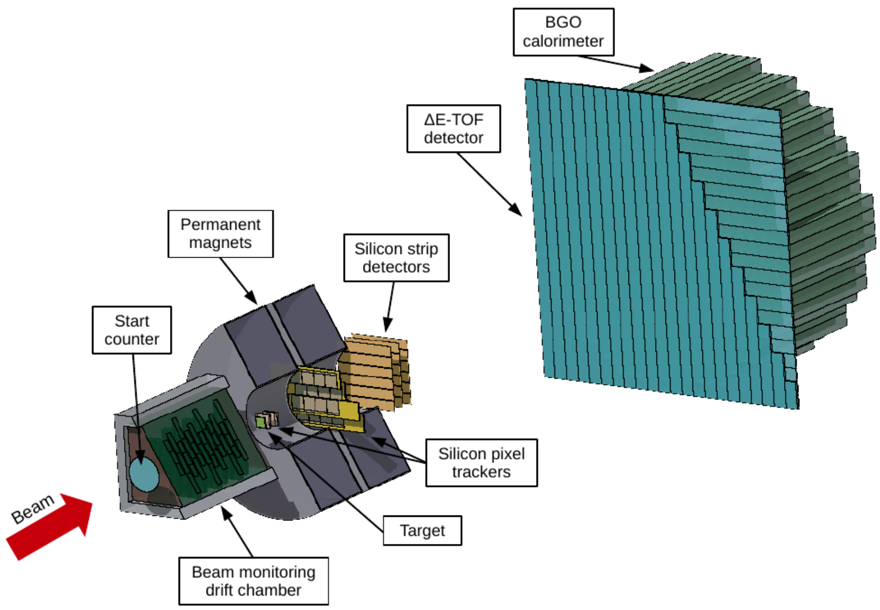

Figure 1: Scheme of the final FOOT apparatus, obtained with FLAIR [11], the FLUKA [12, 13] graphical interface.

the fragments have ranges of the order of tens of μm [4] and have a low probability of leaving the target and being detected. To overcome this difficulty, the FOOT experiment uses an inverse kinematic approach. Rather than accelerating therapeutic proton beams onto biological targets, FOOT studies the fragmentation of accelerated beams of ions composing the human body (e.g., carbon and oxygen) onto an hydrogen-enriched target. In the inverse reference frame, fragments have a boost in energy and thicker targets can be used. The incident beam flux will be set so as the projectile rate will be low enough (few kHz) to have only one particle at a time crossing the system.

The FOOT apparatus is schematically shown in Fig. 1. The beam enters the left of the system and crosses the start counter, a plastic scintillator read by silicon photomultipliers (SiPMs) that provides the trigger information and the first timestamp of the time-of-flight (TOF) measurement. The beam profile is then reconstructed by means of the beam monitoring drift chamber that measures the direction and impact position of the ion beam on the target, necessary for an inverse kinematic approach. The vertex, trajectory and momentum of the fragments are measured after the target by a tracking system composed of a series of silicon detectors around and inside a dedicated magnetic spectrometer. The tracking system allows matching the reconstructed tracks with the hits in the last two elements in the detection chain, a ΔE-TOF detector and a calorimeter. The ΔE-TOF detector measures the ΔE, i.e., the energy deposited in a plastic scintillator, and the second timestamp of the TOF, i.e., the arrival time of the particle. The BGO calorimeter measures the kinetic energy of the fragments. The FOOT detector is optimized for the measurement of the heavier fragments mainly produced in the angular range of ±10 degrees with respect to the beam direction. For the detection of the lighter fragments, the experimental setup changes completely, substituting all the apparatus after the drift chamber with an emulsion spectrometer divided in three sections, which measure the charge, energy and mass of the fragments, respectively.

The final goal of the FOOT experiment is to measure the differential production cross section with 5% uncertainty for ions beams impinging onto different targets. For this purpose, the produced fragments should be identified with 1-2 MeV/u resolution in the fragment kinetic energy (after applying the inverse Lorentz transformation) and with ∼10 mrad accuracy in angle.

The ΔE-TOF detector contributes to the particle identification by providing the velocity β of the crossing fragments, which can be obtained by the TOF, and the atomic number Z, since the deposited energy ΔE is proportional to Z^2. The detector is based on plastic scintillators read by silicon photomultipliers (SiPM) [14, 15]. Plastic scintillators are particularly advantageous because they are fast, can be easily shaped based on custom requirements and have long attenuation length. They are appropriate for charged particle detectors because they are capable to reveal minimum-ionizing-like particles with a few mm thick detectors. SiPMs are smaller than conventional photomultiplier tubes, thus being more suitable for the coupling to thin bars, and the combination of plastic scintillator bars to SiPMs is also cost-effective.

The ΔE-TOF detector of the FOOT apparatus will be composed of two layers of plastic scintillator bars, arranged orthogonally and read by silicon photomultipliers controlled with dedicated electronics. The two layers of orthogonal bars in the ΔE-TOF detector will measure the coordinates in the transverse plane of the interaction position of each fragment in the scintillator. For this measurement, multiple fragments that belong to the same event and interact simultaneously in the bar are an issue, because the multiple fragments cannot be distinguished and cause a mis-reconstruction of the coordinates.

The dimensions of the bars and of the detector are determined by various constraints. Since the ΔE-TOF detector will be placed at approximately 1 m from the vertex of production of the fragments, an area of 40 cm×40 cm is required to match the angular aperture of the heavier fragments at this distance. A bar width of 2 cm limits the occurrence of double fragments in the same bar below a few percent level and matches the transversal dimension of the cells of the calorimeter, which the ΔE-TOF detector will be mechanically coupled to. The thickness of the bars will be chosen as a compromise between the amount of scintillation light produced in the bar (which increases with the deposited energy and therefore with the bar thickness), and the contamination of the ΔE-TOF measurement by spurious events of fragmentation in the bar, which also increases with the bar thickness, and whose effects on the FOOT apparatus performance are still under investigation. Each bar will be 2-3 mm thick, 2 cm wide and 40 cm long, and each layer will be composed of 20 bars. To meet the FOOT experiment final requirements, the ΔE-TOF detector should achieve resolutions $\sigma_{\Delta E}/\Delta E \sim 2-3\%$ and $\sigma_{TOF} \sim 70$ psec in ΔE and TOF measurements, respectively [9].

To investigate the performance of the ΔE-TOF detector, a small prototype composed of a single bar coupled to SiPMs was developed. This prototype was characterized in terms of energy, time and spatial resolution, using protons of various energies in the range 70-230 MeV and impinging onto different points along the bar. The energy and time response of the prototype were evaluated as a function of the proton position to investigate the capability to unambiguously reconstruct the fragment interaction position in the case of multiple fragments. In the FOOT experiment, the information of the calorimeter can be used to solve the ambiguity on the position of the fragments. However, the capability of the ΔE-TOF detector to reconstruct the position without the information coming from other detectors can simplify the data managing during the acquisition and the elaboration phases.

The paper is organized as follows. Section 1 describes the developed prototype detector and the data acquisition system, the experimental setup for the proton test beam, and the methods for the data post-processing and analysis. Section 2 reports the energy resolution as a function of the proton interaction position and energy, the time resolution at different proton energies, the description of the detector response and the reconstruction of the proton interaction position. In Sec. 3 we discuss the prototype performances and propose possible improvements for the next prototype version. The conclusions of this study are summarized in Sec. 4.

1. Materials and Methods

1.1. ΔE-TOF detector prototype

The ΔE-TOF detector prototype was composed of a 20 cm × 2 cm × 0.2 cm plastic scintillator bar (EJ212, Eljen Technology, Sweetwater, Texas). The two ends were polished and each end was optically coupled to two 3 mm × 3 mm SiPMs (ASD-NUV SiPMs, AdvanSiD, Trento, Italy). The two SiPMs at each extremity were connected in series in order not to degrade the time performance of the photo-detector by reducing the total capacitance [16]. The remaining four sides of the bar were wrapped with three layers of white diffusive Teflon to increase the amount of collected light and with an external black tape layer to

Table 1: Specifications of the plastic scintillator (from [17]) and silicon photomultipliers (from [18]) used in the ΔE-TOF detector prototype. OV stands for overvoltage above the SiPM breakdown value.

EJ212	Light yield	10^4 ph/MeV
	Light emission peak	423 nm
	Mean attenuation length	250 cm
	Rise time	0.9 ns
	Decay time	2.4 ns
NUV SiPM	Cell size	40 μm
	Fill factor	60%
	Dark count rate (20°C, 6 V OV)	100 cps/mm^2
	Photon detection efficiency (420 nm)	43%
	Recharge time	70 ns
	Single photon time resolution (5 V OV)	270 ps [19]

ensure light-tightness. The specifications of the plastic scintillator and SiPMs are summarized in Table 1.

1.2. DAQ system

The ΔE-TOF detector trigger and data acquisition system (TDAQ) is based on the WaveDAQ system developed in collaboration by PSI and INFN [20]. In this study, we used a WaveDREAM board (WDB, i.e., the first layer of a WaveDAQ system), which is fully programmable and capable to acquire 16-channels. The WDB provides 16 input channels with variable gain amplification and flexible shaping by means of a programmable pole-zero cancellation. Switchable gain-10 amplifiers and programmable attenuators allow an overall input gain from 0.5 to 100 after conversion of the signal amplitude to voltage. Two Domino Ring Samplers (DRS4 chips, [21]) are connected to two 8-channel ADCs, which are read out by a Field-Programmable Gate Array (FPGA). The DRS chip is a waveform digitizer with programmable sampling speed from 1 to 5.12 Gsamples/s (GSPS). The onboard Cockcroft-Walton-based power supply was used to bias the SiPMs.

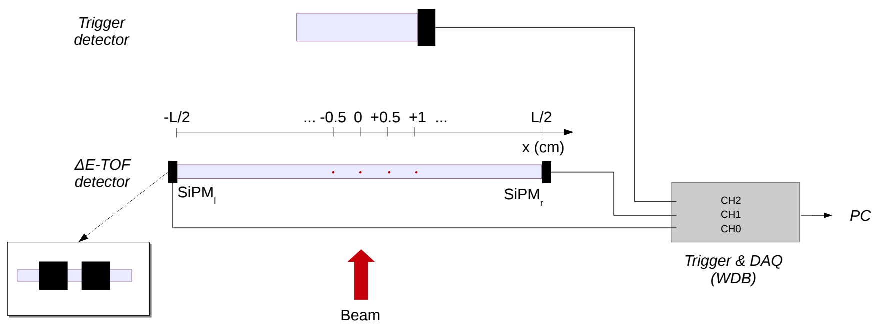

Figure 2: Scheme of the ΔE-TOF detector and trigger and data acquisition system. The center of the bar corresponds to the position $x = 0$. The SiPMs on the left (right) are denoted by SiPM$_l$ (SiPM$_r$). Some of the proton interaction positions are indicated.

1.3. Experimental setup

The prototype was characterized at the Proton Therapy Centre of the Trento Hospital (PTC, Trento, Italy). The experimental setup is schematically shown in Fig. 2. The beam line provided a pencil beam with Gaussian profile and variable energy [22]. The ΔE-TOF detector was placed 85 cm from the exit window. At this distance, we expect from Ref. [22] a beam size of approximately 3-7 mm standard deviation for the various proton energies, in particular 3.5 mm at 170 MeV. The trigger detector, a plastic scintillator read-out by a photomultiplier tube, was placed at a distance of 18 cm. The output of the trigger detector was sent to an input channel of the WDB. In this paper, the center of the bar corresponds to the position $x = 0$. The SiPMs on the left (right) are denoted by SiPM$_l$ (SiPM$_r$). In each measurement, the SiPMs were biased 5 V above the breakdown value (26.7 V), and the sampling speed of the acquisition system was set to the maximum available rate (5.12 GSPS).

To evaluate the dependence of the energy and time resolution on the proton energy, a scan in the range $E_p = 70 - 230$ MeV was performed, with protons at $x = 0$ cm. Table 2 reports, for a given proton energy E_p, the mean and standard deviation of the deposited energy ΔE in the bar, estimated with FLUKA [12]

Table 2: Mean and standard deviation of the deposited energy ΔE in the prototype scintillating bar for a given proton energy E_p. The subscript L stands for Landau fluctuations contribution.

Proton Energy E_p (MeV)	**ΔE (MeV)**	**$\sigma_L(\Delta E)$ (MeV)**
70	2.09	0.125
75	1.98	0.124
80	1.88	0.120
90	1.71	0.118
110	1.47	0.110
140	1.25	0.098
170	1.11	0.085
200	1.02	0.078
230	0.94	0.074

Monte Carlo simulations. In addition, the dependence of the energy resolution on the proton interaction position x was estimated by translating the detector with 0.5 cm steps, with $E_p = 170$ MeV.

1.4. Data analysis

Waveform processing. Figure 3 shows two example waveforms obtained in the following conditions: interaction position $x = +2.5$ cm, proton energy $E_p = 170$ MeV, voltage amplification of 2.5. The mean pedestal was calculated by averaging the last 60 points before the signal leading edge, and it was subtracted from each point of the waveform. We assumed that the energies collected by the left and the right SiPMs E_l and E_r were proportional to the time integrals of the corresponding waveforms. The total collected energy E_{l+r} was their sum, obtained after rescaling the two contributions to be equal in $x = 0$. The integrals were then converted to the number of triggered SiPM cells by dividing them by the time integral of a single cell signal.

The timestamps of the left and right SiPMs ($t_{l,r}$) and of the trigger detector (t_{trig}) were obtained with the constant fraction discriminator (CFD) method, i.e., by selecting the timestamp when the signal amplitude crossed a predetermined fraction of its maximum amplitude. The waveform sampled at 5.12

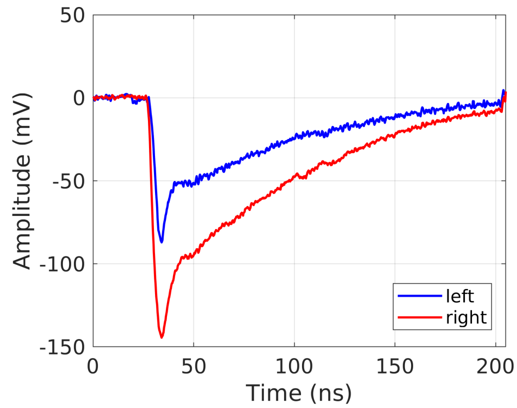

Figure 3: Example of waveforms acquired at the two sides of the bar, with a $E_p = 170$ MeV proton at $x = +2.5$ cm, voltage amplification of 2.5, and after subtraction of the pedestal level.

GSPS, ie. approximately every 200 ps, was interpolated to a 1 ps sampling step.

Energy resolution. The energy resolution was calculated as the ratio of the standard deviation and the mean of the collected energy, for the two ends of the bar and for the total collected signal ($E_{l,r,l+r}$). For the proton energy scan, the contributions of the Landau fluctuations in the deposited energy ΔE and of the statistical fluctuations in the number of detected photons were estimated. The fluctuations in the deposited energy were provided by the Monte Carlo simulations (Table 2) and were subtracted in quadrature from the total energy resolution. The number of detected photons was estimated as the number of triggered SiPM cells divided by the SiPM excess charge factor ($ECF = 2$ for the used SiPMs at 5 V overvoltage [23]).

Time resolution. The detector time resolution was obtained as the standard deviation of the distribution of $(t_l - t_r)$, fitted with the following function:

$$f(E) = \sqrt{\frac{S^2}{E} + C^2} \tag{1}$$

where E in this case is the deposited energy, and S and C are the fit parameters. The detector time performance was also tested with the trigger detector. The detector timestamp $t_{det} = (t_l + t_r)/2$ was calculated for each event to obtain the time of flight $TOF = t_{det} - t_{trig}$, and the TOF time resolution $\sigma(TOF)$ was defined as the standard deviation of the TOF values, given by a Gaussian distribution fit.

Light attenuation in the bar. Due to the attenuation of optical photons in the bar, the collected energy at the two ends of the bar is a function of the proton interaction position, and a model of the optical attenuation allows to uniform the energy response of the detector. The collected energies $E_{l,r,l+r}(x)$ were described with exponential functions of the interaction position, as suggested in [24]:

$$f_l(x) = A_l \exp\left(-\frac{L/2 + x}{\lambda}\right), \quad f_r(x) = A_r \exp\left(-\frac{L/2 - x}{\lambda}\right) \tag{2}$$

and $f_{l+r}(x) = f_l(x) \cdot N_l + f_r(x) \cdot N_r$, where $L = 20$ cm is the bar length, x is the distance of the interaction position from the center of the bar, λ is the effective attenuation length of the bar over the scintillator emission spectrum, the multiplicative factors $A_{l,r}$ are constants for the two ends of the bar, accounting for possible differences in the photo-detectors gain, and $N_{l,r}$ are the normalization factors that make the two responses equal at the center. The energy resolution as a function of the collected energy $E_{l,r}$ at the different positions was modeled with a function of the form of Eq. 1, where C in this case is due to the intrinsic resolution of the detector and to the fluctuations in the deposited energy, and it is a constant since the proton energy E_p was fixed during the position scan.

Position reconstruction. The proton interaction position can be determined either by the logarithm of the ratio of the collected energies at the two ends of the bar $L_{lr} = \ln\left(\frac{E_l}{E_r}\right)$, or by the difference between the left and right timestamps $T_{lr} = (t_l - t_r)$. The data of the interaction position scan were split into a calibration-set and a test-set. The calibration set was used to create, for each of the two parameters, a look-up-table (LUT) containing the mean value of the parameters for each interaction position. The results were interpolated with a 0.25 cm sampling pitch and extrapolated to the range [-8,+8] cm.

The values of the two parameters were calculated for each event of the test-set, and the position of interaction was then reconstructed by finding the position in the bar that minimized the quadratic sum of the differences between values of the two parameters for a given LUT position and their true value, $\arg\min_{x} \left[(L_{lr}^{LUT}(x) - L_{lr})^2 + (T_{lr}^{LUT}(x) - T_{lr})^2\right]$.

2. Results

2.1. Energy resolution

Figure 4 shows the mean number of triggered SiPM cells at the two ends of the bar as a function of the energy ΔE deposited in the bar with the beam at $x = 0$ (taken from Table 2). The number of triggered cells depends linearly on the deposited energy, with slopes $171{\pm}7$ MeV^{-1} and $152{\pm}5$ MeV^{-1}, respectively for the left and right side, and intercepts 4 ± 10 and 6 ± 8 (adjusted coefficient of determination $R^2_{adj} > 0.99$ [25]).

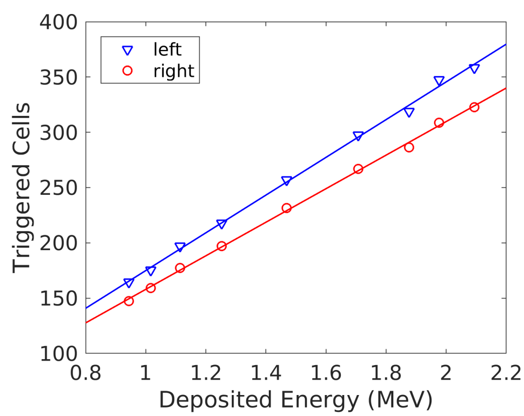

Figure 4: Mean number of triggered SiPM cells as a function of the mean deposited energy ΔE (from Table 2) for the two ends of the bar.

Figure 5 shows the measured energy resolution as a function of the deposited energy (triangles), for the two ends of the bar individually and for the sum of the two, at $x = 0$. The contribution of the Landau fluctuations in the deposited energy was then subtracted (circles). In addition, the contribution of the statistical fluctuations in the number of detected photons (squares) is shown for the two ends only. The energy resolutions obtained after the subtraction of

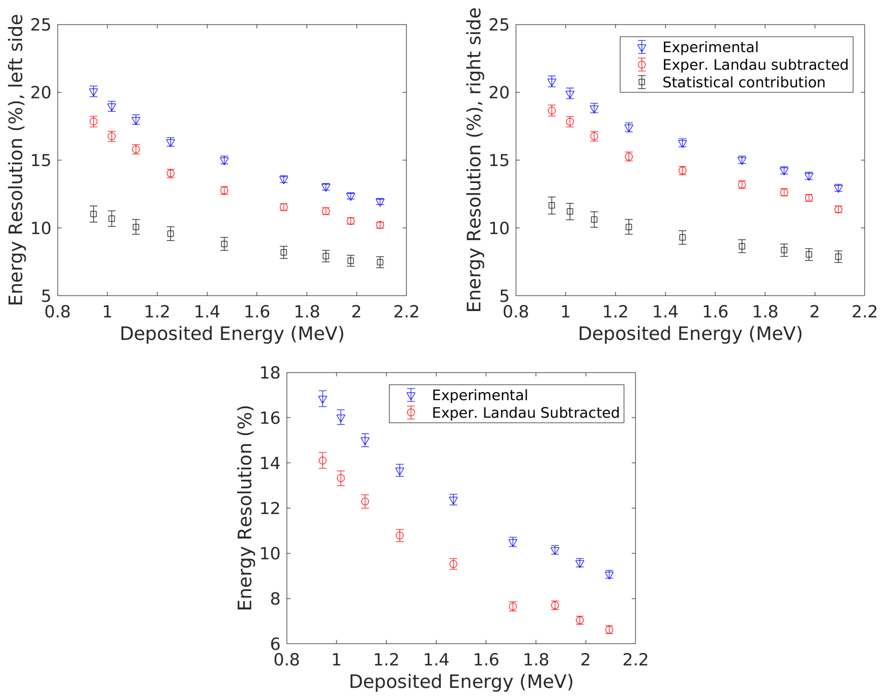

Figure 5: Energy resolution at $x = 0$ as a function of the deposited energy ΔE, for the two ends of the bar (top) and for their sum (bottom), before (triangles) and after (circles) subtraction of the Landau fluctuations. The contribution due to statistical fluctuations of the light yield are shown separately by black squares. Error bars represent the confidence interval at the 95% level.

the Landau contribution do not follow the model of Eq.1. The reasons for this discrepancy are still being investigated, but it could be partially due to the method chosen to estimate the Landau contribution (i.e., evaluating the intrinsic resolution from the Landau asymmetric shape).

2.2. Time resolution

A scan of the CFD threshold indicated that the values that minimize the time resolutions were 10% and 30% of the maximum absolute value of the signal for the ΔE-TOF detector and for the trigger detector, respectively. Figure 6 shows the left-right time resolution $\sigma(t_l - t_r)$ (left) and the TOF time resolution $\sigma(TOF)$ (right) as a function of the deposited energy ΔE. For the left-right time resolution, the fit with Eq. (1) gave $S = 259 \pm 15$ ps$\cdot\sqrt{\text{MeV}}$, and $C = 118 \pm 13$ ps ($R^2_{adj} = 0.99$).

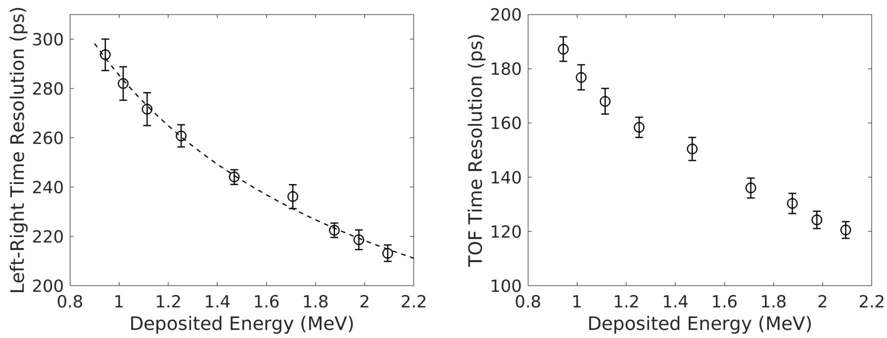

Figure 6: Detector left-right time resolution $\sigma(t_l - t_r)$ and fit with Eq. 1 (left) and TOF time resolution $\sigma(TOF)$ (right) as a function of the deposited energy. Error bars represent the confidence interval at the 95% level.

2.3. Light attenuation along the bar

The mean collected energy as a function of position is shown in Fig. 7, for fixed energy $E_p = 170$ MeV. The values for the individual ends of the bar ($E_{l,r}$) and for the sum of the two (E_{l+r}) are shown with different symbols. Solid lines represent the fits to the data with Eq. (2). The trend is similar for the two SiPM groups, and it is monotonic with the position. The slight fluctuations with position are presumably due to non-uniformities in the scintillator wrapping. The following values for the attenuation length were obtained: $\lambda_l = 12.1 \pm 0.5$ cm and $\lambda_r = 10.7 \pm 0.3$ cm ($R^2_{adj} = 0.99$ for the two ends, $R^2_{adj} = 0.93$ for the sum of the two). The discrepancy between the two values of attenuation length can be due to imperfections in the bar wrapping which make the fit less accurate. A difference of approximately $(A_l - A_r)/A_l \simeq 18\%$ was found between the amplitude of the energy collected at the two ends, and it is presumably due to a different efficiency in the light collection (e.g., coupling, angle between SiPMs and bar edge, SiPM gain).

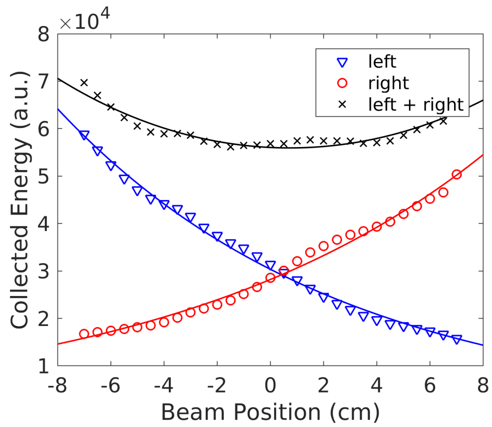

Figure 7: Mean collected energy at the two ends of the bar ($E_{l,r}$) and total collected energy (E_{l+r}) as a function of the position, for the fixed proton energy of 170 MeV. Solid lines represent the fit to the data with Eq. (2).

Figure 8 (left) shows the energy resolution as a function of position, for the individual channels and for the sum of the two. The energy resolution of the

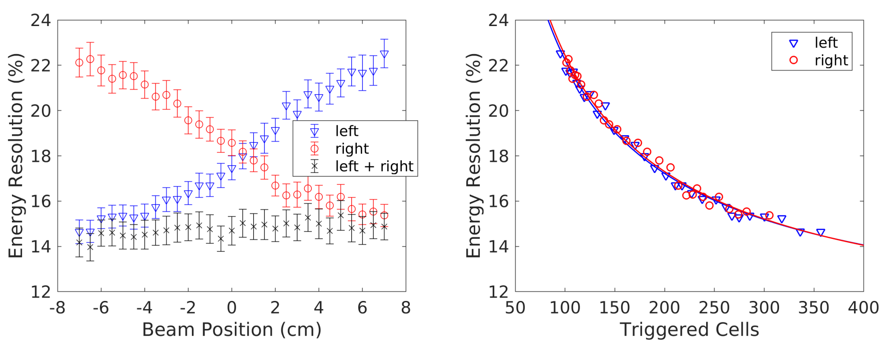

Figure 8: Energy resolution as a function of position (left). Error bars represent the confidence interval at the 95% level. Energy resolution as a function of the mean number of triggered cells at different distances from the photo-detectors (right).

single ends of the bar ranged from 15% when the protons are closer to the SiPMs to 23% when they are farther from the SiPMs. Only a slight difference was noted between the two sides. The energy resolution was approximately constant when the data from the two sides were combined ($\sim$ 14%-15%). Figure 8 (right) presents the energy resolution of the individual ends of the bar as a function of the mean number of triggered cells depending on the interaction position. The fit with Eq. (1) gave the following values: $S_l = 200 \pm 1\ \sqrt{\text{cells}}$, $C_l = 9.9 \pm 0.4$ %, $S_r = 202 \pm 1\ \sqrt{\text{cells}}$, and $C_r = 9.8 \pm 0.4$ % ($R^2_{adj} = 0.99$).

2.4. Position reconstruction

Figure 9 shows the dependence of the logarithm $\ln\left(\frac{E_l}{E_r}\right)$ on the interaction position x. Figure 10 presents the distribution of $(t_l - t_r)$ for some positions (left), and their mean for all positions (right). A slope of 280±20 ps/cm was obtained from the linear fit of the latter. Both figures were obtained at fixed proton energy $E_p = 170$ MeV.

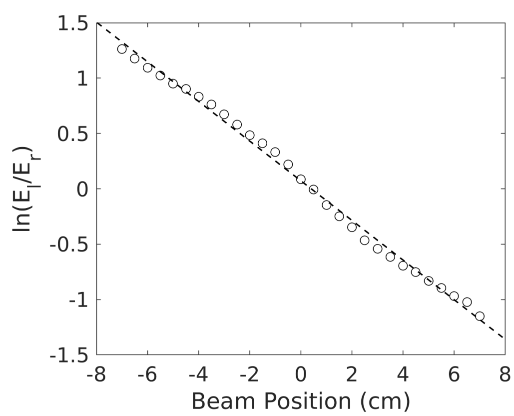

Figure 9: Dependence of the logarithm of the ratio of the collected energies on the interaction position ($E_p = 170$ MeV).

The correlation between $\ln\left(\frac{E_l}{E_r}\right)$ and $(t_l - t_r)$ is shown in Fig. 11 as a scatter plot for three different positions (different colors). The black dots and the white dashed lines indicate the mean and the full-width-at-half-maximum (FWHM) contours of the distributions, respectively.

Figure 12 shows the distribution of the interaction position x reconstructed using the LUT method for 8 beam positions along the bar in the range $[-7, +7]$ cm, separated by 2 cm steps. A spatial resolution of approximately FWHM = 1.9 cm was obtained at the center of the bar. The contribution of the beam spot size

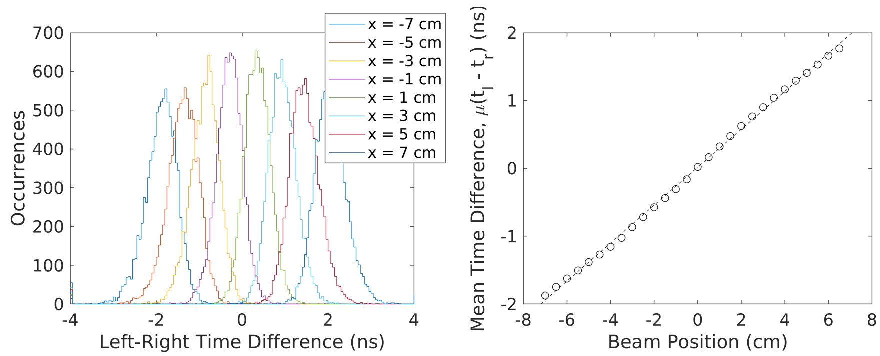

Figure 10: Distribution of the difference between the left and right timestamps $(t_l - t_r)$, for some interaction positions in the bar (left). Mean difference between the left and right timestamps, for all positions (right). The dashed line represents the linear fit to the data. The proton energy was fixed at 170 MeV.

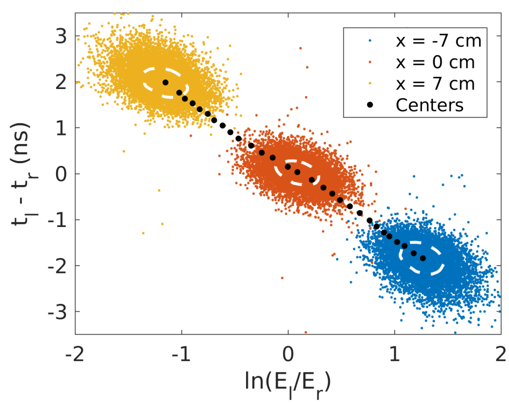

Figure 11: Scatter plot of the difference in the collected energy at the two ends of the bar vs. the difference in the left and right timestamps, $\ln \frac{E_l}{E_r}$ and $(t_l - t_r)$, for three different positions (different colors). The black dots and the white dashed lines indicate the mean and the FWHM contours of the distributions, respectively.

was not subtracted because it is significantly smaller than the detector spatial resolution (see Ref. [22]).

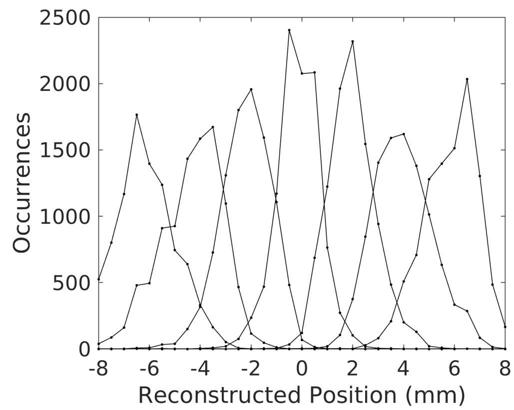

Figure 12: Distributions of the x-coordinate reconstructed using the LUT method for 8 beam positions.

3. Discussion

In this study, the energy, time and spatial resolution of a ΔE-TOF detector were investigated as a function of the particle energy and interaction position inside the detector. The TOF resolution measured with respect to the trigger detector was $\sigma(TOF) = 120$ ps for 70 MeV protons (last point in Fig.6 right). Even if this resolution does not meet the FOOT experiment requirements, we remind that the test was performed with the lightest particles (thus releasing the smallest energy in the scintillator), that the contribution of the trigger detector was not subtracted, and that two layers of bars will be used in the final setup. Therefore, further prototype studies are required to evaluate a potential improvement in the time resolution of the final ΔE-TOF detector.

An energy resolution of 10-11% was obtained with 70 MeV protons on each side of the bar, after subtracting the Landau fluctuation contribution. The statistical fluctuations of the number of detected photons contribute with an energy resolution of approximately 8%, whilst the residual contribution is partially due to the SiPM crosstalk [26], afterpulse and electronic noise. Combining the information at the two ends of the bar, an energy resolution of approximately 6.5% was obtained after subtracting the Landau contribution. In the final detector, the two layers of plastic scintillator bars will provide two measurements of the deposited energy, with a consequent resolution improvement. In addition, aspects to be investigated are, for example, the effects of the optical coupling between the plastic bar and the SiPMs, the angle between SiPMs and bar edge, the differences in the SiPM gain. Furthermore, to increase the amount of collected light, the next prototype will feature 4 SiPMs connected in series at each extremity. In this case, the alignment of the different detector components will be even more relevant.

Proton beams were chosen to characterize the detector performance because they produce the smallest amount of scintillation light in the bar, thus providing the worst case scenario. They also represent the simplest case because they do not fragment in the bar. However, due to the small amount of deposited energy, they did not allow to investigate the saturation effects in the SiPMs. Based on Monte Carlo simulations, we expect deposited energies up to $\sim$100 MeV, according to the fact that the deposited energy is proportional to Z^2. Therefore, assuming no scintillator quenching for high deposited energies, the detector must be capable of detecting 2 orders of magnitude more photons than in the current irradiations. The detector prototype has $11250 = 2 \cdot 5625$ cells at each end, and 150-350 were triggered with 70-230 MeV protons. Therefore, we expect some saturation effects with heavy ions such as C or O. Although the photo-detector saturation can be calibrated to linearize the detector response, this effect degrades the energy resolution. A possible solution which will be investigated in the future is the use of smaller cells.

The results of this study show that the response of the detector as a function of the particle interaction position can be analytically described (Fig. 7). An attenuation length of approximately 11-12 cm was obtained by scanning the central region of the 20 cm long bar. These results indicate that the attenuation in the final 40 cm long detector will significantly reduce the light collection efficiency. This aspect will be improved by replacing the diffusive reflector around the bars with a specular reflector, and could be improved also by using 3 mm thick bars. With the proposed method for the interaction position determination (Fig. 12), the final detector ΔE-TOF will be able to discriminate multiple particles interacting simultaneously in two pairs of bars, because a spatial resolution (FWHM = 1.9 cm) comparable with the detector granularity was achieved. This result was obtained at the center of the bar and for 170 MeV protons. The spatial resolution could degrade closer to the SiPMs due to the lower light yield from the far end of the bar.

4. Conclusions

In this study, the energy, time and spatial resolution of a ΔE-TOF detector composed of a plastic scintillator bar readout at both ends by SiPMs were investigated using protons of different energies interacting at different positions in the plastic scintillator bar. The detector response was linear with the deposited energy in the investigated proton energy range (70-230) MeV. With 70 MeV protons, an energy resolution of approximately 6.5% was obtained after subtracting the Landau contribution, and a time resolution of 120 ps was achieved in coincidence with a reference detector. The energy resolution obtained by combining the data at the two ends of the bar was independent from the particle interaction position within $\pm 1\%$ in the studied range $[-7, +7]$ cm. The results of this study provided useful indications to improve the ΔE-TOF detector performances in order to meet the requirements of the FOOT experiment. The particle interaction position in the bar was reconstructed with a spatial resolution comparable to the width of the plastic scintillator bars, allowing to discriminate two fragments generated by the same particle.

References

[1] G. Kraft, Tumor therapy with heavy charged particles, Progress in Particle and Nuclear Physics 45 (2000) S473–S544.

[2] M. Durante, H. Paganetti, Nuclear physics in particle therapy: a review, Reports on Progress in Physics 79 (9) (2016) 096702.

[3] A. C. Kraan, Range verification methods in particle therapy: underlying physics and Monte Carlo modeling, Frontiers in Oncology 5 (2015) 150.

[4] F. Tommasino, M. Durante, Proton radiobiology, Cancers 7 (1) (2015) 353–381.

[5] R. Pleskac, Z. Abou-Haidar, C. Agodi, M. Alvarez, T. Aumann, G. Battistoni, A. Bocci, T. Böhlen, A. Boudard, A. Brunetti, et al., The FIRST experiment at GSI, Nuclear Instruments and Methods in Physics Research Section A: Accelerators, Spectrometers, Detectors and Associated Equipment 678 (2012) 130–138.

[6] J. Dudouet, D. Juliani, M. Labalme, D. Cussol, J. Angélique, B. Braunn, J. Colin, C. Finck, J. Fontbonne, H. Guérin, et al., Double-differential fragmentation cross-section measurements of 95 MeV/nucleon 12C beams on thin targets for hadron therapy, Physical Review C 88 (2) (2013) 024606.

[7] M. Toppi, Z. Abou-Haidar, C. Agodi, M. Alvarez, T. Aumann, F. Balestra, G. Battistoni, A. Bocci, T. Böhlen, A. Boudard, et al., Measurement of fragmentation cross sections of C12 ions on a thin gold target with the FIRST apparatus, Physical Review C 93 (6) (2016) 064601.

[8] FOOT Conceptual Design Report, `https://pandora.infn.it/public/912bb8` (accessed on 2018/01/11).

[9] V. Patera, et al., The FOOT (Fragmentation Of Target) Experiment, PoS (2017) 128.

[10] G. Battistoni, et al., The FOOT (Fragmentation Of Target) Experiment, PoS (2017) 023.

[11] V. Vlachoudis, et al., FLAIR: a powerful but user friendly graphical interface for FLUKA, in: Proc. Int. Conf. on Mathematics, Computational

Methods & Reactor Physics (M&C 2009), Saratoga Springs, New York, 2009.

[12] A. Ferrari, P. R. Sala, A. Fasso, J. Ranft, FLUKA: A multi-particle transport code (Program version 2005), Tech. rep. (2005).

[13] T. Böhlen, F. Cerutti, M. Chin, A. Fassò, A. Ferrari, P. Ortega, A. Mairani, P. R. Sala, G. Smirnov, V. Vlachoudis, The FLUKA code: developments and challenges for high energy and medical applications, Nuclear data sheets 120 (2014) 211–214.

[14] P. Marrocchesi, O. Adriani, Y. Akaike, M. Bagliesi, A. Basti, G. Bigongiari, S. Bonechi, M. Bongi, M. Kim, T. Lomtadze, et al., Beam test performance of a scintillator-based detector for the charge identification of relativistic ions, Nuclear Instruments and Methods in Physics Research Section A: Accelerators, Spectrometers, Detectors and Associated Equipment 659 (1) (2011) 477–483.

[15] M. De Gerone, A. Bevilacqua, M. Biasotti, G. Boca, P. Cattaneo, F. Gatti, M. Nishimura, W. Ootani, G. Pizzigoni, M. Rossella, et al., A high resolution Timing Counter for the MEG II experiment, Nuclear Instruments and Methods in Physics Research Section A: Accelerators, Spectrometers, Detectors and Associated Equipment 824 (2016) 92–95.

[16] P. W. Cattaneo, M. De Gerone, F. Gatti, M. Nishimura, W. Ootani, M. Rossella, Y. Uchiyama, Development of high precision timing counter based on plastic scintillator with SiPM readout, IEEE Transactions on Nuclear Science 61 (5) (2014) 2657–2666.

[17] Eljen Technology Plastic scintillators, `http://www.eljentechnology.com/products/plastic-scintillators/ej-200-ej-204-ej-208-ej-212` (accessed on 2018/01/11).

[18] C. Piemonte, F. Acerbi, A. Ferri, A. Gola, G. Paternoster, V. Regazzoni,

G. Zappala, N. Zorzi, Performance of NUV-HD silicon photomultiplier technology, IEEE Transactions on Electron Devices 63 (3) (2016) 1111–1116.

[19] M. Nemallapudi, S. Gundacker, P. Lecoq, E. Auffray, Single photon time resolution of state of the art SiPMs, Journal of Instrumentation 11 (10) (2016) P10016.

[20] A. Baldini, E. Baracchini, C. Bemporad, et al., The design of the MEG II experiment, Eur. Phys. J. C 78 (2018) 230.

[21] S. Ritt, The DRS chip: Cheap waveform digitizing in the GHz range, Nuclear Instruments and Methods in Physics Research Section A: Accelerators, Spectrometers, Detectors and Associated Equipment 518 (1) (2004) 470–471.

[22] F. Tommasino, M. Rovituso, S. Fabiano, S. Piffer, C. Manea, S. Lorentini, S. Lanzone, Z. Wang, M. Pasini, W. Burger, et al., Proton beam characterization in the experimental room of the Trento Proton Therapy facility, Nuclear Instruments and Methods in Physics Research Section A: Accelerators, Spectrometers, Detectors and Associated Equipment 869 (2017) 15–20.

[23] F. Acerbi, A. Ferri, G. Zappala, G. Paternoster, A. Picciotto, A. Gola, N. Zorzi, C. Piemonte, Nuv silicon photomultipliers with high detection efficiency and reduced delayed correlated-noise, IEEE transactions on Nuclear Science 62 (3) (2015) 1318–1325.

[24] F. Ciocia, A. Braem, E. Chesi, R. De Leo, C. Joram, L. Lagamba, E. Nappi, J. Séguinot, I. Vilardi, P. Weilhammer, GEANT4 studies on the propagation and detection of scintillation light in long thin YAP crystals, Nuclear Instruments and Methods in Physics Research Section A: Accelerators, Spectrometers, Detectors and Associated Equipment 600 (2) (2009) 506–512.

[25] A. Srivastava, V. Srivastava, A. Ullah, The coefficient of determination and its adjusted version in linear regression models, Econometric reviews 14 (2) (1995) 229–240.

[26] S. Vinogradov, T. Vinogradova, V. Shubin, D. Shushakov, K. Sitarsky, Probability distribution and noise factor of solid state photomultiplier signals with cross-talk and afterpulsing, in: Nuclear Science Symposium Conference Record (NSS/MIC), 2009 IEEE, IEEE, 2009, pp. 1496–1500.